Miniature particulate matter counter and analyzer based on lens-free imaging of light scattering signatures with a holed image sensor

Gabriel Jobert, Pierre Barritault, Maryse Fournier, Salim Boutami, Daphnée Jobert, Adrien Marchant, Julien Michelot, Paul Monsinjon, Pierre Lienhard, Sergio Nicoletti

▶ **To cite this version:**

Gabriel Jobert, Pierre Barritault, Maryse Fournier, Salim Boutami, Daphnée Jobert, et al.. Miniature particulate matter counter and analyzer based on lens-free imaging of light scattering signatures with a holed image sensor. Sensors and Actuators Reports, 2020, 2, pp.100010. 10.1016/j.snr.2020.100010 . cea-04530281

HAL Id: cea-04530281
https://cea.hal.science/cea-04530281v1

Submitted on 3 Apr 2024

HAL is a multi-disciplinary open access archive for the deposit and dissemination of scientific research documents, whether they are published or not. The documents may come from teaching and research institutions in France or abroad, or from public or private research centers.

L'archive ouverte pluridisciplinaire **HAL**, est destinée au dépôt et à la diffusion de documents scientifiques de niveau recherche, publiés ou non, émanant des établissements d'enseignement et de recherche français ou étrangers, des laboratoires publics ou privés.

Distributed under a Creative Commons Attribution - NonCommercial - NoDerivatives 4.0 International License

Sensors and Actuators Reports 2 (2020) 100010

Contents lists available at ScienceDirect

Sensors and Actuators Reports

journal homepage: www.elsevier.com/locate/snr

Miniature particulate matter counter and analyzer based on lens-free imaging of light scattering signatures with a holed image sensor

Gabriel Jobert [a,*], Pierre Barritault [a], Maryse Fournier [a], Salim Boutami [a], Daphnée Jobert [a], Adrien Marchant [a], Julien Michelot [b], Paul Monsinjon [b], Pierre Lienhard [b], Sergio Nicoletti [a]

[a] CEA-LETI Minatec, Université Grenoble-Alpes, F38000 Grenoble, France
[b] Pyxalis, Moirans, France

ARTICLE INFO

Keywords:
Air quality
Particulate matter sensor
Light-scattering
CMOS image sensor
Lens-free imaging
Image processing

ABSTRACT

We report our latest developments on a novel miniature particulate matter (PM) sensor for personal air quality monitoring. This optical sensor combines a visible fibered light source and a vertical air channel drilled out of a holed retina. The fabrication of such retina features an unconventional design of a CMOS image sensor and a specific drilling post process at wafer level. The scattering of light by a single particle generates a distinctive pattern. By using a compact optical set-up, we measure a lens-free projection of the scattering signature on the image sensor. We present the design and fabrication of such sensor as well as experimental signatures that are consistent with our in-house analytical model. We demonstrate counting and differentiation between calibrated particles of different sizes. Our current setup allows for the detection of single 320 nm polystyrene particles. Finally, we describe our image analysis procedure that fits a measured signature with a modelled one in order to retrieve particle's size and refractive index.

1. Introduction

1.1. Particulate Matter and low-cost monitors

Fine Particulate Matter (PM) is a distribution of suspended objects (solids or liquids) which sizes range from a few nanometers to a few micrometers. Hazardous media such as heavy metal toxicants or mutagenic substances may compose PMs which are known to have a serious impact on health [1,2], in particular on cardiovascular, cardiac and respiratory diseases such as lung cancer. A causal relationship has been demonstrated between premature death and exposure to PM [3].

Reports have shown that the finer a particle is, the deeper it penetrates the human respiratory system (up to the alveolar duct for the 100 nm particles) [4]. Regulatory texts rank PM into subclasses according to their size. In particular, subclass $PM_{2.5}$ (particles smaller than 2.5 μm) have been classified as a known carcinogenic agent (group 1) by the International Agency for Research on Cancer (IARC) [5,6]. Additionally, unregulated subclass PM_1 (submicronic particle) is expected to be far more harmful than $PM_{2.5}$ [7,8].

As air quality is becoming a major issue of concern, low-cost, portable and personal air quality monitors are clearly needed [9–11]. Indeed, conventional air quality monitoring ground stations with costly and bulky equipment [12], or satellite based observation [13] are not suited neither for high spatiotemporal monitoring of outdoor pollution nor for the monitoring of indoor air quality [14,15].

Among a vast field of techniques that can be used to detect fine particles [16], optical sensors based on the light scattering phenomenon appears to be the best candidates for miniaturized systems thanks to their good sensitivity and simplicity.

The light scattering technique is used in the vast majority of low cost $PM_{2.5}$ monitors [17]. It consists of a single light source (visible or near infrared) that illuminates an air channel where a particle can deviate a part of light accordingly to the principle of light scattering. A single photodetector is placed in an off-axis configuration and is able to detect only the scattered light [18]. Such setup is illustrated in Fig. 1.

Great efforts are being made within the scientific and technical communities to scale down optical PM2.5 & PM1 sensors using similar setups. It usually involves silicon microfabrication techniques and co-integration of light sources, passive optics, photodetectors and fluidics [19–21].

Fig. 1 illustrates the simplest light-scattering setup. It is able to estimate the total concentration of PM but is insensitive to the nature and size distribution of the particles from the sampled aerosol. In most cases, a particle filtering stage can be used prior to the optical measurement unit, allowing for example the sensitivity to $PM_{2.5}$, excluding PM_{10}. Particle filtering can be efficiently achieved by taking advantage of their

* Corresponding author.

https://doi.org/10.1016/j.snr.2020.100010
Received 23 March 2020; Revised 10 April 2020; Accepted 27 April 2020
Available online 11 May 2020
2666-0539/© 2020 The Author(s). Published by Elsevier B.V. This is an open access article under the CC BY-NC-ND license. (http://creativecommons.org/licenses/by-nc-nd/4.0/)

Please cite this article as: G. Jobert et al., Miniature particulate matter counter and analyzer based on lens-free imaging of light scattering signatures with a holed image sensor, Sensors and Actuators Reports (2020), https://doi.org/10.1016/j.snr.2020.100010

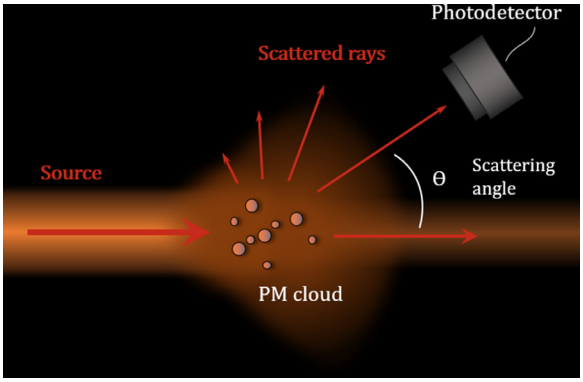

Fig. 1. Illustration of the light-scattering technique.

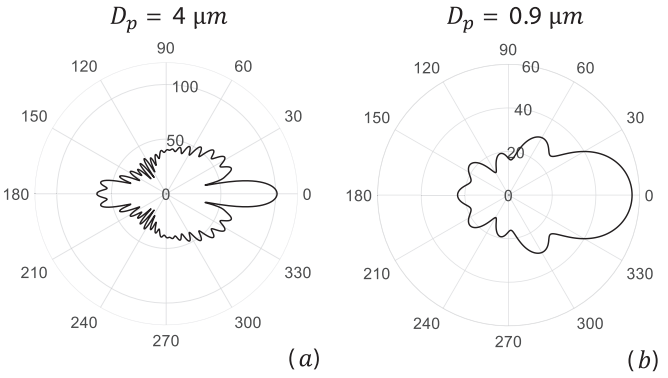

Fig. 2. Scattering signatures of PSL spheres of two different diameters: (a) 4 µm and (b) 0.9 µm.

inertial proprieties: it is used in fluidic set-up like virtual impactors (VI) [22] and cyclones [23] to cite only a few.

It is also possible to estimate optical parameters such as refractive index and sphere equivalent diameter by retrieval and analysis of the light scattering proprieties of an aerosol: for example by multi-wavelength illumination [24] or discrete multi-angle scattering [25,26] measurements. Other light-scattering sensors aims to measure the complete angular scattering efficiency function by using either a rotating detection arm [27,28] or an array of photo detectors coupled with an optical Fourier transform optical set-up using mirrors [29] or lenses [30].

Optical Particle Counters (OPC) usually function the same way as those light-scattering sensors [31], the difference being that only one particle should be detected at a time. It usually requires focusing optics or particle focusing nozzles to limit the detection area [32] as well as high numerical aperture detection optics. The size can then be estimated using the scattering intensity of a single particle. These OPC are generally calibrated and can accurately size particles within a small range of refractive indexes, however this limitation can be mitigated by evaluating an optimized field of view of scattering angle [33]. Another family of OPCs allows the counting and classification using an lens-less/holographic set-up [34–36].

The sensor described in this manuscript is able to measure the 'light scattering signature' (angular scattering efficiency) of a single particle using a lens-less imaging set-up. This technique is designed to be able to estimate the diameter and the refractive index of a particle. The Lorenz–Mie theory describes very well such signature for spherical particles, allowing us to identify a particle through its optical and geometrical parameters.

1.2. Brief introduction to Lorenz–Mie theory and scattering signatures

One can predict the absorbed optical power and the scattered intensity as a function of the scattering angle (the angle between the illumination axis and the scattered light) by knowing parameters such as particle shape, size and refractive index, and illumination conditions. In order to perform the inverse problem, which is to determine the nature of an aerosol (through its optical and geometrical properties), it is crucial to be able to measure this angle-dependent scattering efficiency, we call 'particle scattering signature' [37].

A common description of the phenomenon of light scattering is the Lorenz–Mie theory [38,39]. The latter is a solution of Maxwell's electromagnetic equations for a sphere of homogeneous complex refractive index, illuminated by a monochromatic plane wave and is valid for any range of diameter.

Fig. 2 shows the scattering signatures (polar plots with a logarithmic scale) of laboratory PolyStyrene Latex (PSL) spherical particles with two different diameters.

These signatures were calculated using our in-house Lorenz–Mie calculator with a non-polarized incident plane wave of wavelength $\lambda = 635$ nm onto a single PSL sphere with refractive index $n_{PSL} = 1.5875$ at this wavelength [40]. We show that coarse particles (few wavelengths of diameter) present several scattering angular lobes of higher intensity. The number of these lobes decreases with the particle diameter and is highly dependent on the particle refractive index.

The Lorenz–Mie theory is well suited for spherical particles (such as calibrated laboratory particles, suspended droplets, wood fire, some microbiological species etc.), but may not be applied to model particles with irregular shapes found in ambient air. Others generalized theories can be used to model non-spherical particles [41–44].

2. Architecture of the sensor

2.1. General design

We present in Fig. 3, a schematic rendering of the architecture of the sensor.

The sensor is composed of a holed retina (CMOS image sensor) mounted on a holed ceramic and driven by an electronic board. The vertical traversing hole works as a fluidic channel where an aerosol is set in motion by an external forced convection.

Particles are illuminated by the light beam formed by a lensed fiber placed nearby the muzzle of the channel. The fiber is mounted onto a 3D-printed piece designed as a 'cloaker', preventing stray-light blooming of the focal plane.

Finally, we measure a lens-less projection of the scattered signature of a single particle on the holed retina. Then the resulting image can be numerically processed.

2.2. Dual matrixes Global Shutter Imager chip

We have developed a CMOS imager chip customized for our special requirements [45], as explained later, our unusual design will allow us to drill a hole through the chip to form the fluidic channel [46]. Our chip was modified from the CreaPYX standard platform proposed by the

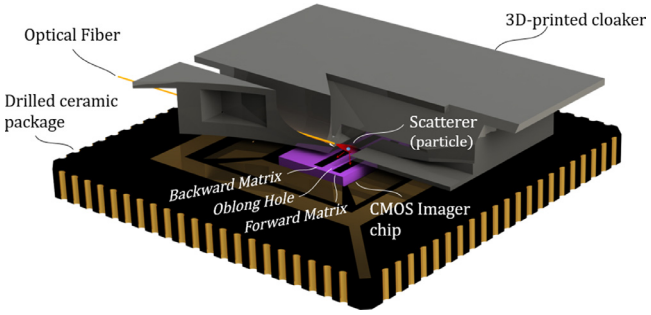

Fig. 3. Architecture of the sensor (partial cross-sectional view).

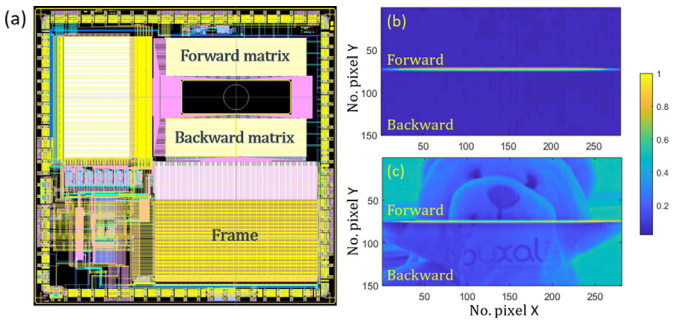

Fig. 4. (a) Imager chip layout. Image example in (a) flat-field mode and (c) focus mode.

Pyxalis company [47]. The former is designed in a prototyping fashion: flexible and rapidly modified with limited effort and at lower cost.

We present the layout in Fig. 4(a). The imager is composed of a classic frame part and an uncommon dual matrixes core part. This core part has two detection areas ('forward' and 'backward matrix') separated by a central blind area. These matrixes are labelled according to the direction of the scattered light they assess: forward scattering and backscattering. Both matrixes are sized by 75 × 281 pixels, with a pitch of $p_{pix} = 10\ \mu m$. The blind area between the two detection matrixes is sized by 2160 µm × 660 µm (rectangular profile) and is made free of pixels or metallic lines (and thus, ready to be drilled).

We show examples of images obtained in flat-field and focus modes in subfigures 4(b) and (c), respectively. X and Y labels are the pixel numbers, all the following images will be presented with this format, lines from 1 to 75 and lines from 76 to 150 correspond respectively to the forward and backward matrixes. We observe saturated hot pixels at the internal edges (central bright lines), caused by a higher dark current. For the image processing, we simply ignore these eight defective lines.

The pixel is designed with a 2 gains high dynamic range, 5T architecture allowing a low noise Global-Shutter (GS) readout procedure [48]. Unlike the common Rolling Shutter mode where each line is captured sequentially, Global Shutter mode allows to capture the full image simultaneously. Since the particle is moving, the latter mode is essential to prevent motion blurring or distortion of the image. The Charge-to-Voltage Conversion Factor (CVF) is 120 µV/e- in high gain mode and the gain is 45 µV/ADU (Analog to Digital Unit). Such pixel design is well suited for capturing low intensity scattering signatures with good sensitivity.

2.3. Post-process and packaging

The imager chips were fabricated on 200 mm wafers that were supplied from a shuttle run of a specialized advanced CMOS manufacturing fab. Then, we have developed a post-process in our in-house 200 mm MEMS foundry to drill the components at wafer scale (see [45] for further details). We present the final holed retina in Fig. 5.

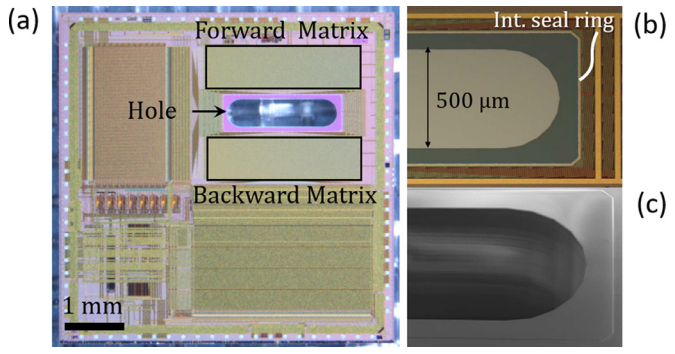

Fig. 5. Images of the fabricated holed retina. (a) Optical view of the chip. (b) Optical view zoomed on the hole. (c) Tilted SEM view of the hole.

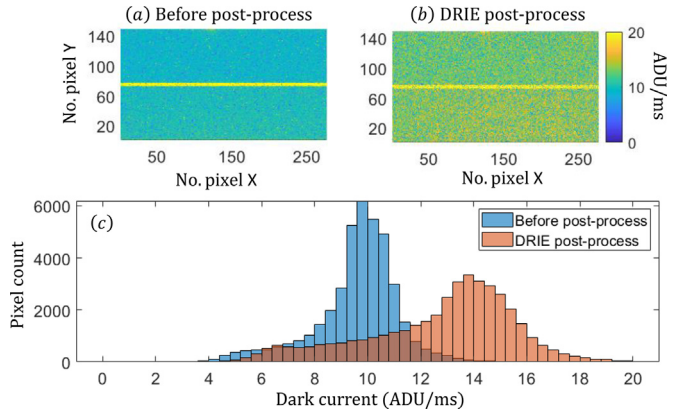

Fig. 6. Cartography of the dark current (in ADU/ms) before (a) and after (b) the drilling post-process, and associated histograms (c).

The layout includes an alignment mark for our lithography steps. An external seal ring is commonly used around the chip. Here, we also added an internal seal ring around the hole area designed to protect the matrix of photodetectors during the drilling process.

The first step concerns a front-side process that etches the multilayer passivation with an oblong profile (2 mm x 0.5 mm). To do so, we use a C_4F_8/CO plasma process in a Reactive Ion Etching (RIE) reactor. We finalize the etching of the air channel by a backside process. We deposit a few microns of oxide hard mask by PECVD and use a contact photolithography on a positive resin to pattern the oblong profile. In order to achieve a fast, deep anisotropic etching of 725 µm, we use an Inductively Coupled Plasma-Deep Reactive Ion Etching (ICP-DRIE) [49]. The ICP reactor is widely used for anisotropic silicon etching because it maintains vertical sidewalls with high aspect ratio. In our case, a standard Bosch process (cyclic isotropic etching with SF_6 gaz followed by C_4F_8 plasma) is sufficient to obtain a straight profile as our aspect ratio $AR = 1.45$ is not particularly tricky.

We will simply use the term DRIE to refer to this etching process. Fig. 5(b) shows an optical image of the hole. Fig. 5(c) shows a tilted scanning electron microscope (SEM) image of the hole demonstrating the very high quality of the DRIE process.

In order to estimate the impact of the post process on the dark current (DC) of the image sensor, we made dark current maps before (Fig. 6 (a)) and after the DRIE step (Fig. 6(b)). We acquire dark images for increasing integration time $I_d(t_{int})$ expressed in ADU (AnalogToDigitalUnit). We can obtain a DC map by taking the slope map $DC = dI_d/dt_{int}$ expressed in ADU/ms.

Histograms shown in Fig. 6(c) show that the drilling post-process have increased the DC level by about 30%. Fortunately, there is no evidence of gradient in noise distribution: the post-process didn't increased the dark currents in the vicinity of the drilled area. Finally, we should emphasize that the dark current increase is not a critical parameter for our application because we use short integration time.

The chip was wire-bonded (ball bonding) to a ceramic carrier. We have drilled a circular hole (2 mm diameter) through the thickness of the ceramic, which is larger than the hole of the silicon chip (2 mm x 0.5 mm oblong profile). Such fluidic profile eases the convection of the air flow through the channel and creates a flow acceleration at the channel restriction (flowing from the larger ceramic hole to the smaller silicon hole) by a Venturi effect. The ceramic is clipped, with full contact on the socket of the driving motherboard (CreaPYX test platform [47]).

The footprint of the system is limited by the size of the ceramic carrier (square: 29.2 mm) while the size of the silicon chip is only 6 mm x 5.9 mm. Future packaging of this sensor will include direct bonding of the CMOS chip on PCB to reduce the footprint. Compact packaging should include a compact convection system that uses a

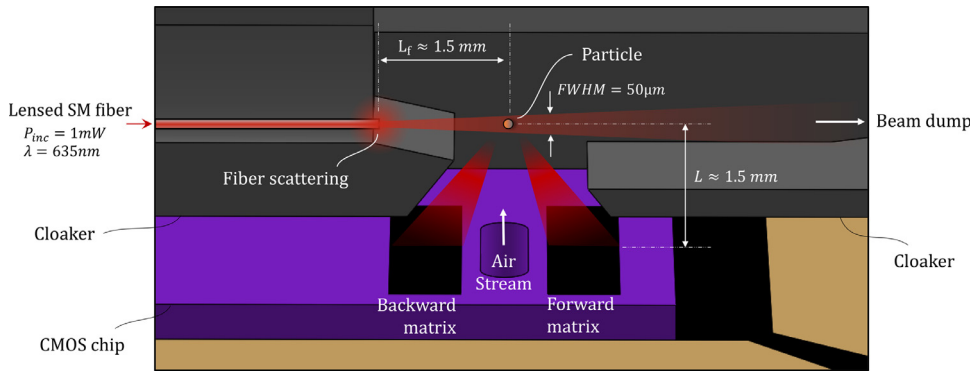

Fig. 7. Schematic of the optical setup

miniature fan. We can also optimize the fluidic set up by designing a nozzle-like channel profile to concentrate the beam of particles while speeding them.

2.4. Optical setup

We illuminate a detection volume nearby the muzzle of the channel at a good proximity of $L \approx 1.5$ mm between the optical axis and the retina. This proximity allows for a good sensitivity to scattered light (as the scattered intensity decreases with the inverse square of the viewing distance) and a quite wide field of view of scattering angles.

The illumination beam is shaped by a single mode optical fiber terminated by a GRIN lens. The beam, thus obtained has a very low numerical aperture of 0.02. The fiber is connected to a visible light source ($\lambda = 635$ nm, SLED from EXALOS), delivering the optical power $P_{inc} = 1$ mW at the fiber output. We have selected this wavelength because it shows the best compromise between the scattering efficiency and the prices of the sources. Figure 7 illustrates the optical setup.

The optical fiber is aligned and mounted on a multipurpose 3D-printed piece we call a 'cloaker', which primary purpose is to protect the focal plane from stray light as much as possible. In particular, scattered light from the output of the optical fiber can easily bloom the retina, making the sensor completely dazzled and thus blind to scattered light from particles.

The cloaker is fabricated with a black resin using a high-resolution (25 µm voxel) stereo-lithography 3D printer (Form 2 printer by Formlabs). Fig. 8 shows a photography of the cloaker side by side with its 3D model.

Developments on the next-generations optical set-up features miniature molded optics for beam shaping from an emitting surface (such as LEDs), removing the need for the bulky fiber. In an alternative architecture geometry, we can perform an optical pre-treatment of the scattering

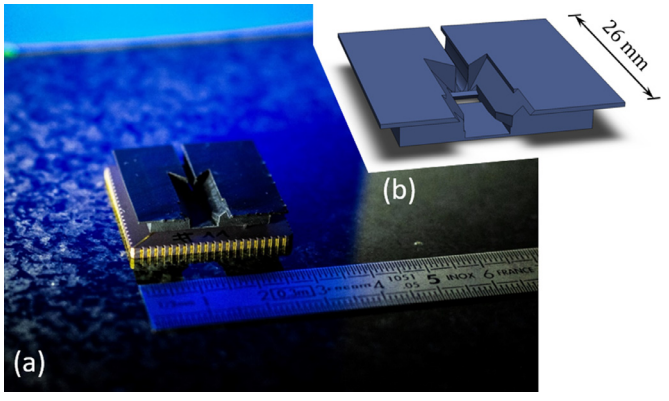

Fig. 8. (a) Photography of the chip mounted on ceramic with the cloaker. (b) 3D model of the cloaker.

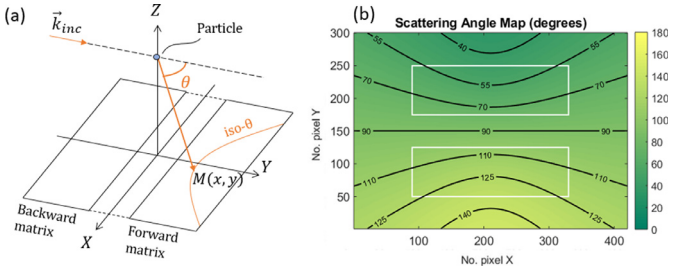

Fig. 9. (a) Schematic of the scattering projection. (b) Calculated map of projected scattering angles.

signature similar to our wide FoV, Fourier-domain imaging miniature optics designs [50,51].

3. Analytical modelling of the lens free projection

3.1. Generalities and definitions

The output of the fluidic channel (along Z axis) is illuminated by a light beam ($\vec{k}_{inc}$) at a short distance of the retina ($L \approx 1.5\ mm$), see Fig. 9 (a).

To calculate the scattering of the incident light by the particle, we use the Lorenz–Mie theory locally: this is a local electromagnetic description where the particle is spherical and illuminated by a plane wave. Then, we perform a near-field/far-field transformation so that we can consider scattered light as rays. These scattered rays are cast from the position of the particle (now considered punctual) and projected onto the retina under a scattering angle θ. The signature is carried along perpendicular trajectories to what we call 'iso-θ', meaning 'the curve where all the pixels are illuminated under the same scattering angle'. In the case of a planar projection parallel to the optical axis of illumination, which corresponds to our configuration, the 'iso-θ' are hyperbolae as shown in the calculated scattering angles map in Fig. 9(b).

The white rectangles correspond to the 'forward' and 'backward' detection areas where we can evaluate the scattering signatures. Here, we define the Field of View (FoV) as the range of evaluated scattering angles. In this case, each submatrix can evaluate scattering signatures within a FoV of about 25 degrees.

3.2. Radiometric model

We present in Fig. 10, the calculated projection (using our in-house radiometric model described in Appendix A) for the 4 µm and 0.9 µm PSL presented in Fig. 2.

As before, white rectangles correspond to the imaging regions defined by the 'forward' and 'backward' matrixes. We observe that the lobes seen in the scattering signature are projected into luminous arcs

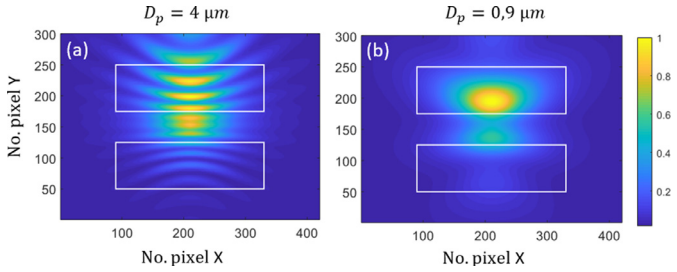

Fig. 10. Calculated planar projection of scattering signatures for particle diameters of (a) 4μm and (b) 0.9μm.

that follow the 'iso-θ' hyperbolae. For simplicity, 'iso-θ' will now refer only to maxima and minima of theses hyperbolae. These projections well justify the relevance of the planar projection technique for scattering signature analysis as we can see a clear difference between the two images.

4. Characterization Results

4.1. Experimental setup and protocol

We generate a controlled flow of particles using a calibrated aerosol dispenser (Constant Output Atomizer Model 3076 by TSI). For the particles, we use calibrated laboratory particles (PSL from MagSphere) with monodisperse distribution of particle diameter. These particles are diluted in ultra-pure water solutions, one solution by diameter. The concentration of each solution is chosen in order to detect one particle at a time in our experimental setup, see below.

A portion of the particle flow is directed toward a reference sensor (APS Spectrometer 3321 by TSI) while the rest is sent to our sensor under test, via a silicone tube, with a flow rate of 0.8 L/min. The silicone tube is plugged onto the back of the holed ceramic so that the aerosol flow can traverse through the entire holed device toward the illumination beam. Illuminated particles can scatter light onto the two detection matrixes.

We record the projected scattering signatures using the CreaPYX electronic board [47]. This driving board is interfaced with a standard PC through a USB connection and controlled with a tailored driving software. All images are integrated over time $t_{int} = 5$ ms and automatically subtracted with a background image (which was previously recorded with no particle in the illumination beam).

The electronic board allows for the collection of a pack of 32 images in burst mode (i.e. with maximal framerate) before transferring this pack to the computer and collecting a new burst. Each pack is automatically analyzed with a homemade routine, which consists in a threshold detection, as illustrated in Fig. 11. We monitor the standard deviation of the forward matrix of each image. When no particle crosses the optical beam, the standard deviation remains under the threshold value set by the user. If the threshold is reached, then it is likely that a particle was detected. The corresponding image is saved for subsequent image processing.

For a given particles' diameter, we measure the detection rate f which is the fraction of images that passed the detection threshold over

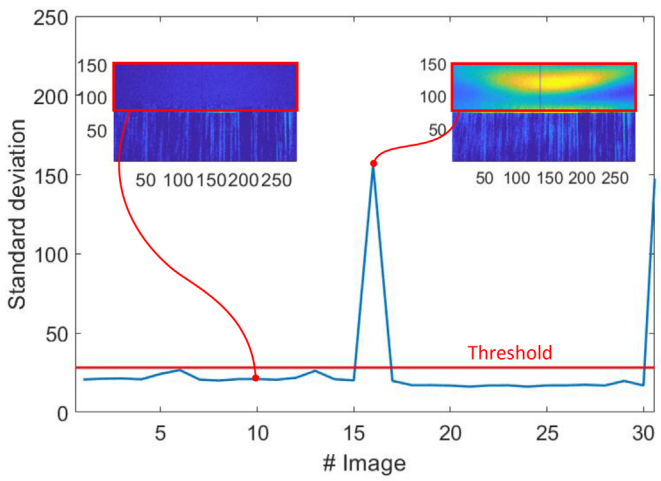

Fig. 11. Example of threshold detection of a single particle.

the total of images recorded. For example, we obtained a detection rate of $f_{PSL3} = 0.074$ for 3 μm PSL particles. As explained before, the particle's concentration is chosen so that we obtain a detection rate much lower than one, thus avoiding double detection issues. These experimental conditions are close to what can be found in outdoor air. This detection rate is the statistical metric that allows us to estimate particle concentration, as these two quantities are presumably linearly equivalent. Note that we consider particle number concentrations (particles/cm^3) instead of the historical (regulated) particle mass concentration (μg/cm^3), as epidemiologists consider the former as a more relevant health metric [52].

4.2. Experimental signatures

We routinely collect bursts of images for different particle concentrations and different PSL diameters. To illustrate the various signatures measured, we present in Fig. 12, a set of four representative signature measurements corresponding to 4 different PSL diameters.

We can see, in Fig. 12, important signature variations with respect to the particle diameter: For small particles (compared to the wavelength), the signature appears spherical as in subfigure (d). Then, as the PSL diameters increases, forward scattering takes an elliptical shape (subfigure (c)) and divides into an increasing number of iso-θ. For particles of a few wavelengths in diameter, the backward matrix starts collecting useful information, in the form of iso-θ (subfigure (a) and (b)). These observations are consistent with our model's predictions (Fig. 10). All images were normalized, as we encountered an important variability in the overall scattered intensity. We will discuss this variability in the next section.

It is noteworthy that the detection of a single submicronic particle down to $D_p = 320$ nm is possible. To go further, it is very likely that smaller PSL could be detected, nevertheless their signature would be very similar to the one of PSL 320 nm. Indeed, for small particles, the iso-θ can't be seen anymore (however we can still evaluate the ratio of the forward/backward intensity). The use of shorter illumination

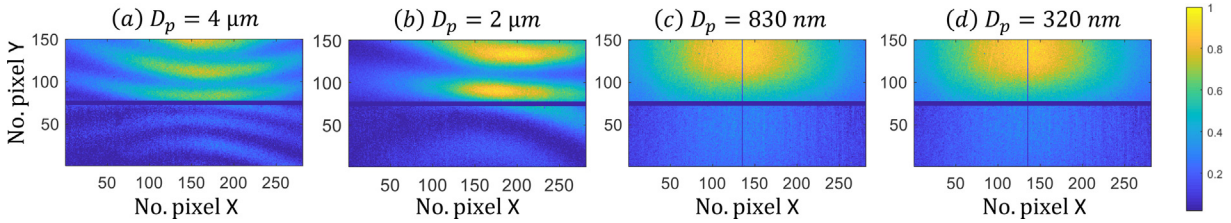

Fig. 12. Experimental detection for four PSL diameters: (a) 4 μm, (b) 2 μm, (c) 830 nm, (d) 320 nm.

wavelength could be a way to bring back iso-θ to smaller diameters in addition to allowing greater sensitivity.

It should be stated that one of the main experimental difficulties we encountered is the important variability of the signatures obtained for each diameter of PSL. Indeed, in our experimental setup, the position and velocity of a particle when it crosses the optical beam can vary. This results in a translation of the signature along the optical axis or a variation of the overall scattering intensity. We will develop this argumentation in the next section since this variability impacts the image processing.

We would like to clarify that the characterizations presented in this section were performed with calibrated laboratory particles that shows scattering patterns that are in great accordance with the Lorenz–Mie theory. The data processing method is designed to work with scattering signatures from spheres as it is well suited for our laboratory characterizations with PSL. In ambient air conditions, most particles have irregular shape and will most likely scatter light in different ways. In the future, we hope to perform characterizations in ambient air with new iterations of our sensor. In order to analyze signatures from real particles, further developments of image processing will have to be made.

5. Image processing

5.1. Strategies for diameter and refractive index retrieval

We explore the ways experimental images can be fitted to modeled images obtained with our radiometric model for given particle diameter D_p and refractive index n. These target particles parameters are variables among other geometric parameters ($x_p, y_p, z_p, \alpha, \beta$) defined in Appendix A, that we need to fit as well.

Within our experimental setup where we use a collimated fiber for illumination, we have found that some parameters have negligible effects (y_p, z_p, α). The effect of a small β can be easily retrieved by evaluating the rotation of the image. The only geometrical parameter we have to fit is the position of the particle along the optical axis (y_p).

Noteworthy, other team that are also working on scaled-down PM sensors have also reported errors induced by the position of the particle [53]. Here, we propose to correct these errors within our image analysis procedure.

Our strategies consists in focusing only on the iso-θ (ridge and valleys only) and define a reduced image contained in a small matrix (see Appendix B). We then define a minimization criterion based on the comparison between reduced images of experimental and modeled signatures (see Appendix C). Minimizing this criterion allows us to estimate particle parameters such as its diameter.

It should be stated that, with our current set-up. We encounter experimental variability in the overall scattered intensity mainly due to particle position and spatio-temporal illumination non-uniformities. Thus, we are not able to use the overall intensity in our data processing method, at least with our current set-up.

5.2. Experimental versus modeled comparison of reduced images: Diameter fit

The diameter of the particle is the metric we want to measure. In our laboratory measurements, we used PSL spheres of refractive index $n_{PSL} = 1,5875$ at our working wavelength [40]. Using our minimization criterion $\varepsilon(D_p)$, we found $D_p = 3.81$ μm. In Figure 13, we present the comparison of the experimental image used in the example and the fitted modeled image.

This test case is presented only to illustrate the principles of the image processing.

Note that the expected diameter was $D_p = 3$ μm (error is 27%). The diameter we have found with our procedure is slightly beyond the scope of the dispersion guaranteed by the supplier of PSL spheres (10%). This error might be due toan unknown combination of the errors from the procedure (and the model) but also the dispersion of the refractive index

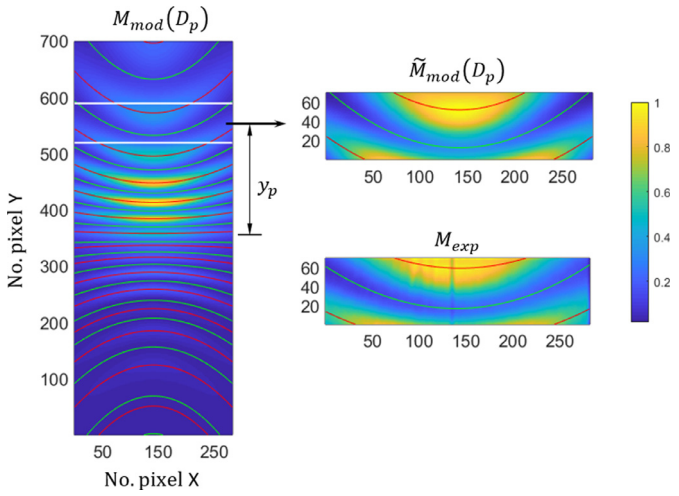

Fig. 13. Example of diameter fit using iso-θ curves.

of PSL. Indeed, it has been found that the refractive index of commercially available polystyrene beads can vary from a sphere to another as shown in reference [54]. Moreover, other teams performing a similar inverse problem as ours also measure a certain distribution in the refractive index [55].

5.3. Sensitivity to refractive index

In Fig. 14, we evaluate our minimization criterion $\varepsilon(D_p, n)$ for a reasonable range of diameters and refractive indices. The experimental image used for the comparison is the same as the one presented before in Fig. 13.

We observe that the reasonable diameter and refractive index we expect from our experimental image are within a local minimum circled in white in the $\varepsilon(D_p, n)$ map shown in Fig. 14. However, other local minima may introduce large errors in the estimation of our parameters.

In future developments, we hope to erase these unwanted local minima by a number of improvements. For example, we could investigate better definitions for $\varepsilon(D_p, n)$; identify relevant parameters to be integrated into our image reduction matrix; pre-estimate the diameter and refractive index using the scattered intensity; implement the

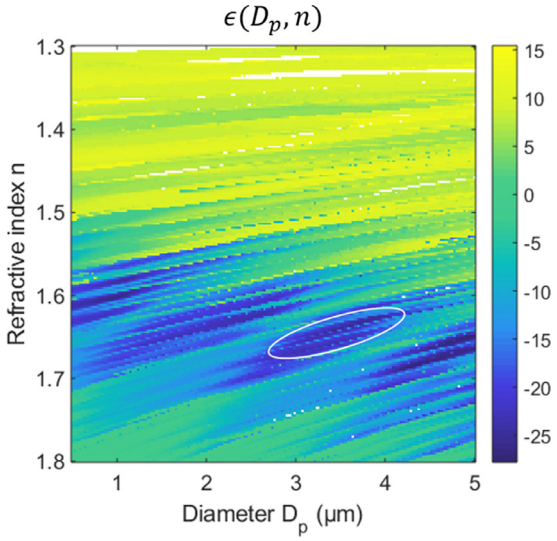

Fig. 14. Map of our minimization criterion against particle diameter and refractive index in logarithmic scale.

simultaneous analysis of both forward and backward matrixes etc. Optimizations within our fluidic set-up could also reduce the range of accessible particle position, improving the precision of the procedure. This procedure will also have to be tested with a large number of test cases to conclude on its accuracy.

We also notice that the region with refractive index inferior to 1.55 has a very high $\varepsilon(D_p, n)$. This suggests that our procedure could differentiate organic media of high refractive index (such as polymers) from inorganic media with a lower refractive index (such as silicates or aqueous droplets). However, one must keep in mind that the procedure must be tested with a large number of test case in order to conclude on its accuracy.

The imaginary part of the refractive index was not considered here, as PSL is not absorbing at the working wavelength. For absorbing particles, the imaginary part should be added to the list of unknowns of this inverse problem.

It should be stated that the method presented in this section is designed to work with spherical particles. Particles present in ambient air can show irregularities in shape that attenuates the effects of the Mie's oscillations [56]. The method is based on the analysis of ridges and valleys found in experimental signatures obtained with spherical laboratory particles, and could not function in its current state with ambient air particles. Future improvements of this method should include more advanced scattering calculators, for instance the T-Matrix method [57], the Finite Difference Time Domain method [44] or machine learning methods [55,58].

6. Conclusion and perspectives

We have presented our latest designs and advances toward the miniaturization of PM sensors.

To make such sensor, we have developed an unconventional design of a CMOS image sensor allowing for a hole drilling post process at wafer level. The hole drilling post process (200 mm CMOS platform) and the packaging are engineered to create a vertical through fluidic channel so that an air stream carrying particles can traverse the sensor. A compact optical set-up featuring a multipurpose, 3D-printed piece we call a cloaker. This enables the alignment of a collimating fiber and protects the focal plane from stray-light. Such optical set-up allows for the lens-free projection of a single particle's scattering signature on the image sensor.

We have developed an analytical model that describes the lens-free projection of scattering signatures that combines the Lorenz–Mie theory and classic radiometric calculations. Experimental images were taken with calibrated laboratory particles (PSL spheres) and show great accordance with our predictions. We have successfully recorded scattering signature of single particles down to a diameter of 320 nm. Finally, we present how we can characterize single particles though image processing using a recorded signature and our model. This image analysis procedure shows great promise retrieving particle diameter and refractive index.

Further developments will include improvements on the packaging: we aim to reduce the footprint of the system by bonding the CMOS chip directly on a compact PCB. The fluidic design with an optimized channel profile and a fan-induced convection would improve both the sensitivity and the image processing precision. The sensitivity and richness of the signatures could be improved by using shorter wavelength and optimized pixels. The next generation optical set up could feature miniature molded optics. Once these modifications applied, we plan to test our sensor with particles more representative of what can be found in ambient air: non spherical particles, metallic, dielectric or organic aggregates. . .To do so, we will definitively have to adapt our image analyses procedure to cope with these morphological variations.

To conclude, we are developing a miniature $PM_{2.5}$ & PM_1 sensor that shows great performances. In the future: after the necessary developments in term of hardware and software, it could be well suited for low cost and portable applications.

Declaration of Competing Interest

The authors declare that they have no known competing financial interests or personal relationships that could have appeared to influence the work reported in this paper.

CRediT authorship contribution statement

Gabriel Jobert: Methodology, Formal analysis, Software, Writing - original draft. **Pierre Barritault:** Methodology, Investigation, Validation, Writing - original draft. **Maryse Fournier:** Methodology, Investigation, Resources, Project administration. **Salim Boutami:** Conceptualization, Formal analysis, Writing - review & editing. **Daphnée Jobert:** Software, Formal analysis. **Adrien Marchant:** Methodology. **Julien Michelot:** Methodology, Resources. **Paul Monsinjon:** Supervision, Resources. **Pierre Lienhard:** Methodology, Resources. **Sergio Nicoletti:** Conceptualization, Writing - review & editing, Funding acquisition.

Acknowledgements

The authors are thankful to the fabrication team of the CEA-Leti for their help concerning the development of the post-process. Lara Boutafa for her works on the packaging. Olivier Lartigue for his expertise on the experimental side. Arnaud Guiot from the CEA's Nano-Safety Platform for his assistance concerning experiments with laboratory particles. Benoit Dupont from Pyxalis for his great implication and support toward the project.

Certain aspects of this work are related to parts of the doctoral activities of the first author that are academically supervised by the University of Lyon. Thus, we wish to thank Cécile Jamois and Christian Seassal for their support and academic supervision.

Appendix A

We describe a radiometric model where the particle is considered as a punctual source with an intensity that varies along the scattering angle, accordingly to a calculated scattering signature (see Lorenz–Mie theory [38], far-field intensity distribution).

First, we normalize the unpolarized far-field distribution of the scattered wave $S(\theta)$ (we call 'scattering signature') by integration over the whole sphere, such as:

$$\int_{\phi=0}^{2\pi}\int_{\theta=0}^{\pi}\left|S(\theta)\right|^2 \sin\theta d\theta d\phi = 4\pi\ sr$$

The intensity of the source (in W/sr) is given by the function $W_{scat}.|S(\theta)|^2$, where W_{scat} is the total scattered intensity calculated using Lorenz–Mie theory.

Second, we need to determine the intensity seen by each pixel of the retina as a function of the scattering angle. We can evaluate the scattering angle θ for every pixel of the retina, following the geometry of Fig. 15.

In our model, the particle can have a certain position $S(x_p, y_p, z_p)$ contained within the volume of the channel and the light beam. The optical axis can be misaligned with respect to Y axis by angles (α, β) delimited by the divergence of the light beam.

For a point $M(x, y)$ in the retina (centered on a pixel), we calculate the associated scattering angle θ and the vignette angle γ. To do so, we define a new set of coordinates (x', y') for the retina transformed with translation by (x_p, y_p) and rotation by β. If $\alpha = 0$ (parallel projection), the associated scattering angle is:

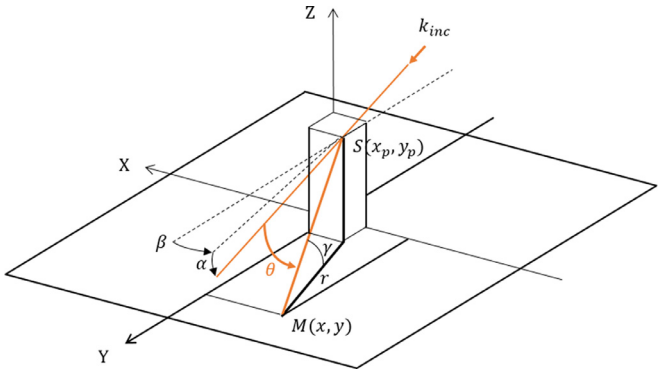

Fig. 15. Geometry of the projection.

$$\theta(M)=\operatorname{acos}\frac{y'}{SM}=\operatorname{acos}\frac{(y-y_p)\cos\beta+(x-x_p)\sin\beta}{\sqrt{(x-x_p)^2+(y-y_p)^2+z_p^2}}$$

Where, SM is the optical length. The case where $\alpha \neq 0$ is left for the reader, who might want to use the Al-Kashi theorem to solve the SFM triangle, F being the intersection of the optical axis and the plane (x', y').

For both cases, the vignette angle γ is given by:

$$\gamma(M)=\operatorname{atan}\frac{z_p}{\sqrt{(x-x_p)^2+(y-y_p)^2}}$$

We define $T(\gamma)$ the angular response of the pixel. This function can be measured or modelled [59]. We also define $\Omega(x, y)$ as the solid angle associated to the pixel centered on $M(x, y)$, explicit expression is:

$$\Omega(x,y)=\frac{FF.\left(p_{pix}\sin\gamma(x,y)\right)^2}{SM^2}$$

Where p_{pix} is the pixel's pitch and FF its filling factor. Finally, the intensity received by the pixel centered on $M(x, y)$ is:

$$I(x,y)=T(\gamma(x,y)).W_{scat}.\left|S(\theta(x,y))\right|^2.\Omega(x,y)$$

The projections we obtain have been compared with ray-tracing (RT) simulations (Zemax Optic Studio, not shown here). Accordance appeared very good. However, we must note that the vignette effects differ from the different methods: the RT method didn't take into account the angular response of pixels while our model uses an angular response calculated from the geometry of the pixel, which is not ideal.

Appendix B

In this appendix, we will discuss how to extract parameters from the iso-θ in order to build the matrix M_{im} that represents the reduced image.

The first step in the recovery of information is the detection of minima and maxima curves (or ridges and valleys). To do this, we go through the columns of the image and recover the positions of the local extrema as shown in Fig. 16(a).

We then recognize the curves, by evaluating the presence of an extremum close from one column to another: if there is, then we consider the two extrema points as part of the same iso-θ. We remove the isolated points, and we automatically connect the pieces of iso-θ truncated by the image, which allows us to model these curves by 2nd order polynomials as shown in Fig. 16(b). Note that this fit is a simplification, as iso-θ are in theory conical curves of the type $a_1X^2+ a_2Y^2+ a_3XY+a_4X+ a_5Y+ a_6=0$. We use the following color code: red for ridges and green for valleys.

Another interesting information that completes the polynomial fit of iso-θ is the width of the iso-θ. L_{iso} is defined as the mean width of the peak at 25% of maximum along the normal at iso-θ, see Fig. 17. The

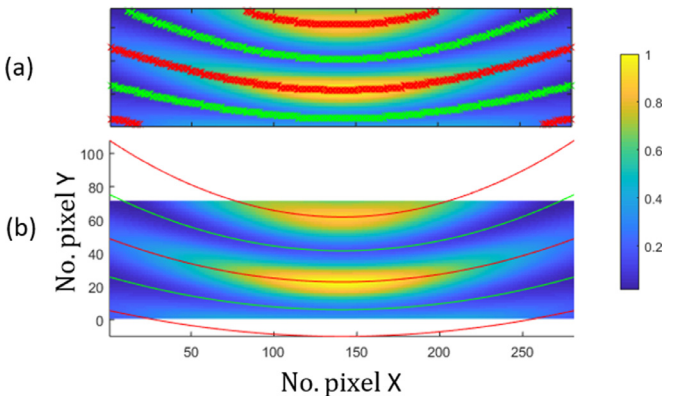

Fig. 16. (a) Detection on extrema, (b) Polynomial fit of iso-θ.

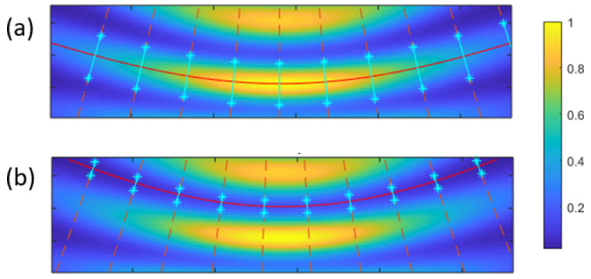

Fig. 17. Recovery of L_{iso} for a ridge (a) and a valley (b).

importance of this information stems from the visual importance we attach to the width of these lobes, which allows us to differentiate images

Then, we define $m=1$ or $m=-1$ depending if the iso-θ is a ridge or a valley. Finally, we build the matrix M_{im} which contains N_{iso} lines that represent all the iso-θ detected (N_{iso} being the number of curves). The columns represent all three 2nd order polynomial fit as well as L_{iso} and m.

$$M_{im}=\begin{bmatrix} P_{2_1} & P_{1_1} & P_{0_1} & L_{iso_1} & m_1 \\ \vdots & & \vdots\ \vdots & & \vdots \\ P_{2_{N_{iso}}} & P_{1_{N_{iso}}} & P_{0_{N_{iso}}} & L_{iso_{N_{iso}}} & m_{N_{iso}} \end{bmatrix}$$

Appendix C

In this appendix, we discuss our strategies used to fit experimental images with modelled ones.

We have observed that the naive strategy of trying to maximize the two-dimensional correlation between experimental and modeled images fails to deliver the expected particle parameters (apart from being computationally heavy). Indeed, the correlation appears to be very sensitive to noise and errors induced by stray light as well as poor modelling of the true vignette effects.

Our chosen strategy consists in comparing simplified images by focusing only on the iso-θ (ridge and valleys only). From an image, either experimental or modelled, we extract relevant information on N_{iso} iso-θ detected such as the curvature and the width of the iso-θ. With these parameters, we can build the matrix M_{im} sized by $(N_{iso} \times 5)$ that represents the reduced image. Details on how we extract theses parameters are reported in Appendix B.

For a given experimental image I_{exp}, we generate modeled images $I_{mod}(D_p, n)$ with the aim of fitting I_{exp}. The modeled image depends on geometrical parameters: in our case, y_p is the only non-negligible parameter. To overcome this dependence, we generate a model with an artificial high number of lines so that the experimental image can be translated vertically to best match the model (horizontal translation,

rotation and magnification can be applied for other geometrical parameters).

The experimental image I_{exp} is reduced into the matrix M_{exp}. In a concern for simplification, we only consider the forward submatrix as it contains sufficient information on the signature.

The large modeled image $I_{mod}(D_p, n)$ is also reduced into the matrix $M_{mod}(D_p, n)$, which generally has a greater number of lines (i.e. more iso-θ detected). In order to compare those matrixes, we crop $M_{mod}(D_p, n)$ to match the size of M_{exp} into several cropped $\tilde{M}_{mod}(D_p, n)$. We exclude comparisons between ridge and valleys, and we keep the cropped matrix that best compares with M_{exp}, which is equivalent to a y_p fit.

The matrix comparison criterion $N_\epsilon(D_p, n)$ is the following:

$$N_{\in}(D_p, n) = \| \left(\tilde{M}_{mod}(D_p, n) - M_{exp} \right) \times D_{pond} \|_2$$

The $\| \cdot \|_2$ stands for the Euclidian norm. D_{pond} is the 5×5 diagonal matrix of ponderation that normalizes each column with M_{exp} and gives a 1/3 ponderation for the columns associated to all three polynomial coefficients. We then calculate $R_2(D_p, n)$, which is the 2D correlation factor between the experimental image and the modeled image translated by the fitted parameter y_p. Finally, we define our minimization criterion:

$$\in(D_p, n) = N_{\in} \times (1 - R_2)$$

References

[1] G.B. Hamra, N. Guha, A. Cohen, F. Laden, O. Raaschou-Nielsen, J.M. Samet, P. Vineis, F. Forastiere, P. Saldiva, T. Yorifuji, D. Loomis, Outdoor particulate matter exposure and lung cancer: a systematic review and meta-analysis, Environ. Health Perspect. (2014), doi: 10.1289/ehp.1408092.

[2] J.O. Anderson, J.G. Thundiyil, A. Stolbach, Clearing the air: a review of the effects of particulate matter air pollution on human health, J. Med. Toxicol. 8 (2012) 166–175, doi: 10.1007/s13181-011-0203-1.

[3] Integrated Science Assessment for Particulate Matter (External Review Draft, 2018), U.S. Environmental Protection Agency, Washington, DC, 2018. https://cfpub.epa.gov/ncea/isa/recordisplay.cfm?deid=341593.

[4] S.A. Cormier, S. Lomnicki, W. Backes, B. Dellinger, Origin and health impacts of emissions of toxic by-products and fine particles from combustion and thermal treatment of hazardous wastes and materials, Environ. Health Perspect. 114 (2006) 810–817, doi: 10.1289/ehp.8629.

[5] A.J. Cohen, J.M. Samet, K. Straif, International Agency for Research on Cancer, Air pollution and cancer, International Agency for Research on Cancer, Lyon, 2013 http://publications.iarc.fr/Book-And-Report-Series/Iarc-Scientific-Publications/Air-Pollution-And-Cancer-2013 .

[6] P. Vineis, K. Husgafvel-Pursiainen, Air pollution and cancer: biomarker studies in human populations, Carcinogenesis 26 (2005) 1846–1855, doi: 10.1093/carcin/bgi216.

[7] V. Howard, Statement of evidence: particulate emission and health (An Bord Plenala, Proposed Ringaskiddy Waste-to-Energy Facility), (2009). http://www.durhamenvironmentwatch.org/Incinerator%20Health/CVHRingaskiddyEvidenceFinal1.pdf (accessed January 3, 2018).

[8] C. Sioutas, R.J. Delfino, M. Singh, Exposure assessment for atmospheric ultrafine particles (UFPs) and implications in epidemiologic research, Environ. Health Perspect. 113 (2005) 947–955, doi: 10.1289/ehp.7939.

[9] E.G. Snyder, T.H. Watkins, P.A. Solomon, E.D. Thoma, R.W. Williams, G.S.W. Hagler, D. Shelow, D.A. Hindin, V.J. Kilaru, P.W. Preuss, The changing paradigm of air pollution monitoring, Environ. Sci. Technol. 47 (2013) 11369–11377, doi: 10.1021/es4022602.

[10] Francesca Borghi, Andrea Spinazzè, Sabrina Rovelli, Davide Campagnolo, Luca Del Buono, Andrea Cattaneo, Domenico Cavallo, Miniaturized monitors for assessment of exposure to air pollutants: a review, Int. J. Environ. Res. Public. Health. 14 (2017) 909, doi: 10.3390/ijerph14080909.

[11] S. Boutami, G. Jobert, P. Barritault, J.-G. Coutard, M. Fournier, J.-M. Fédéli, P. Labeye, A. Marchant, J. Skubich, A. Teulle, O. Lartigue, E. Lorent, A. Glière, C. Constancias, S. Nicoletti, C. Jamois, C. Seassal, L. Duraffourg, Visible to mid-infrared integrated sensors for air quality measurement, in: O. Mitrofanov (Ed.), Opt. Sens. Imaging Photon Count. X-Rays THz 2019, SPIE, San Diego, United States, 2019, p. 25, doi: 10.1117/12.2529262.

[12] P.H. McMurry, M.F. Shepherd, J.S. Vickery, NARSTO (Eds.), Particulate matter science for policy makers: a NARSTO assessment, Cambridge University Press, Cambridge, 2004.

[13] G. Snider, C.L. Weagle, R.V. Martin, A. van Donkelaar, K. Conrad, D. Cunningham, C. Gordon, M. Zwicker, C. Akoshile, P. Artaxo, N.X. Anh, J. Brook, J. Dong, R.M. Garland, R. Greenwald, D. Griffith, K. He, B.N. Holben, R. Kahn, I. Koren, N. Lagrosas, P. Lestari, Z. Ma, J. Vanderlei Martins, E.J. Quel, Y. Rudich, A. Salam, S.N. Tripathi, C. Yu, Q. Zhang, Y. Zhang, M. Brauer, A. Cohen, M.D. Gibson, Y. Liu, SPARTAN: a global network to evaluate and enhance satellite-based estimates of ground-level particulate matter for global health applications, Atmos. Meas. Tech. 8 (2015) 505–521, doi: 10.5194/amt-8-505-2015.

[14] B.C. Singer, W.W. Delp, Response of consumer and research grade indoor air quality monitors to residential sources of fine particles, Indoor Air 28 (2018) 624–639, doi: 10.1111/ina.12463.

[15] S.D. Lowther, K.C. Jones, X. Wang, J.D. Whyatt, O. Wild, D. Booker, Particulate matter measurement indoors: a review of metrics, sensors, needs, and applications, Environ. Sci. Technol. 53 (2019) 11644–11656, doi: 10.1021/acs.est.9b03425.

[16] S. Amaral, J. de Carvalho, M. Costa, C. Pinheiro, An overview of particulate matter measurement instruments, Atmosphere 6 (2015) 1327–1345, doi: 10.3390/atmos6091327.

[17] J. Li, Recent advances in low-cost particulate matter sensor: calibration and application Washington University in St. Louis, 2019.

[18] J.-B. Renard, C. Thaury, J.-L. Mineau, B. Gaubicher, Small-angle light scattering by airborne particulates: environment S.A. continuous particulate monitor, Meas. Sci. Technol. 21 (2010) 085901, doi: 10.1088/0957-0233/21/8/085901.

[19] M. Dong, E. Iervolino, F. Santagata, G. Zhang, G. Zhang, Silicon microfabrication based particulate matter sensor, Sens. Actuators Phys. 247 (2016) 115–124, doi: 10.1016/j.sna.2016.05.036.

[20] S. Nicoletti, Particle detector and method for manufacturing such a detector, EP2596329 B1 2019-03-06 [EP2596329]-EP2596329 A1 2013-05-29 [EP2596329]-WO2012/011052 A1 2012-01-26 [WO201211052]-US8867035 B2 2014-10-21 [US8867035]-US20130120749 A1 2013-05-16 [US20130120749]-US9518909 B2 2016-12-13 [US9518909]-US20150116710 A1 2015-04-30 [US20150116710]-FR2963101 B1 2013-02-15 [FR2963101]-FR2963101 A1 2012-01-27 [FR2963101], n.d. https://permalink.orbit.com/RenderStaticFirstPage?XPN=B5lJYIF%252BxRQ1zTc2PWcWRHf-DUqlXTJ5uwQdFuycu4uk%3D%26n%3D1&id=0&base=.

[21] X. Li, E. Iervolino, F. Santagata, J. Wei, C.A. Yuan, P.M. Sarro, G.Q. Zhang, Miniaturized particulate matter sensor for portable air quality monitoring devices, in: Proceedings of the IEEE Sensors, Valencia, Spain, 2014, pp. 2151–2154, doi: 10.1109/ICSENS.2014.6985464.

[22] O. Mahdavipour, D. Fahimi, I. Paprotny, Microfabricated air-microfluidics virtual impactor with groove-based envelope-flow particle focusing system, in: Proceedings of the 2019 20th International Conference on Solid-State Sensors Actuators Microsystems Eurosensors XXXIII TRANSDUCERS EUROSENSORS XXXIII, Berlin, Germany, IEEE, 2019, pp. 805–808, doi: 10.1109/TRANSDUCERS.2019.8808503.

[23] J. Tryner, C. Quinn, B.C. Windom, J. Volckens, Design and evaluation of a portable $PM_{2.5}$ monitor featuring a low-cost sensor in line with an active filter sampler, Environ. Sci. Process. Impacts. 21 (2019) 1403–1415, doi: 10.1039/C9EM00234K.

[24] S. Wang, X. Xiao, T. Deng, A. Chen, M. Zhu, A Sauter mean diameter sensor for fire smoke detection, Sens. Actuators B Chem. 281 (2019) 920–932, doi: 10.1016/j.snb.2018.11.021.

[25] J.-B. Renard, F. Dulac, G. Berthet, T. Lurton, D. Vignelles, F. Jégou, T. Tonnelier, M. Jeannot, B. Couté, R. Akiki, N. Verdier, M. Mallet, F. Gensdarmes, P. Charpentier, S. Mesmin, V. Duverger, J.-C. Dupont, T. Elias, V. Crenn, J. Sciare, P. Zieger, M. Salter, T. Roberts, J. Giacomoni, M. Gobbi, E. Hamonou, H. Olafsson, P. Dagsson-Waldhauserova, C. Camy-Peyret, C. Mazel, T. Décamps, M. Piringer, J. Surcin, D. Daugeron, LOAC: a small aerosol optical counter/sizer for ground-based and balloon measurements of the size distribution and nature of atmospheric particles – Part 1: Principle of measurements and instrument evaluation, Atmos. Meas. Tech. 9 (2016) 1721–1742, doi: 10.5194/amt-9-1721-2016.

[26] Wenjia Shao, Hongjian Zhang, Hongliang Zhou, Fine particle sensor based on multi-angle light scattering and data fusion, Sensors 17 (2017) 1033, doi: 10.3390/s17051033.

[27] G.W. Mulholland, M.Y. Choi, Measurement of the mass specific extinction coefficient for acetylene and ethene smoke using the large agglomerate optics facility, Symp. Int. Combust. 27 (1998) 1515–1522, doi: 10.1016/S0082-0784(98)80559-6.

[28] G. Kullenberg, Scattering of light by Sargasso Sea water, Deep Sea Res. Oceanogr. Abstr. 15 (1968) 423–432, doi: 10.1016/0011-7471(68)90050-8.

[29] M. Bartholdi, G.C. Salzman, R.D. Hiebert, M. Kerker, Differential light scattering photometer for rapid analysis of single particles in flow, Appl. Opt. 19 (1980) 1573, doi: 10.1364/AO.19.001573.

[30] Y.C. Agrawal, H.C. Pottsmith, Instruments for particle size and settling velocity observations in sediment transport, Mar. Geol. 168 (2000) 89–114, doi: 10.1016/S0025-3227(00)00044-X.

[31] M. Heim, B.J. Mullins, H. Umhauer, G. Kasper, Performance evaluation of three optical particle counters with an efficient "multimodal" calibration method, J. Aerosol Sci. 39 (2008) 1019–1031, doi: 10.1016/j.jaerosci.2008.07.006.

[32] Y.-L. Pan, A. Kalume, C. Wang, J.L. Santarpia, Opto-aerodynamic focusing of aerosol particles, Aerosol Sci. Technol. 52 (2018) 13–18, doi: 10.1080/02786826.2017.1367090.

[33] T. Njalsson, I. Novosselov, Design and optimization of a compact low-cost optical particle sizer, J. Aerosol Sci. 119 (2018) 1–12, doi: 10.1016/j.jaerosci.2018.01.003.

[34] F.C. Cheong, B.S. Rémi Dreyfus, J. Amato-Grill, K. Xiao, L. Dixon, D.G. Grier, Flow visualization and flow cytometry with holographic video microscopy, Opt. Express. 17 (2009) 13071, doi: 10.1364/OE.17.013071.

[35] G. Brunnhofer, A. Bergmann, A. Klug, M. Kraft, Design and validation of a holographic particle counter, Sensors 19 (2019) 4899, doi: 10.3390/s19224899.

[36] Y.-C. Wu, A. Shiledar, Y.-C. Li, J. Wong, S. Feng, X. Chen, C. Chen, K. Jin, S. Janamian, Z. Yang, Z.S. Ballard, Z. Göröcs, A. Feizi, A. Ozcan, Air quality monitoring using mobile microscopy and machine learning, Light Sci. Appl. 6 (2017) e17046, doi: 10.1038/lsa.2017.46.

[37] D. Weinert, T.G. Cleary, G.W. Mulholland, P. Beever, Light scattering characteristics and size distribution of smoke and nuisance aerosols, Fire Saf. Sci. 7 (2003) 209–220.

[38] C.F. Bohren, D.R. Huffman, Absorption and Scattering of Light by Small Particles, Wiley, 1983.

[39] H.C. van de Hulst, Light Scattering by Small Particles, Dover Publications, 1981.

[40] N. Sultanova, S. Kasarova, I. Nikolov, Dispersion properties of optical polymers, Acta Phys. Pol. A. 116 (2009) 585–587, doi: 10.12693/APhysPolA.116.585.
[41] G. Gouesbet, G. Gréhan, Generalized Lorenz–Mie Theories, Springer, Berlin Heidelberg, 2011.
[42] R. Tazaki, H. Tanaka, S. Okuzumi, A. Kataoka, H. Nomura, Light scattering by fractal dust aggregates. I. Angular dependence of scattering, Astrophys. J. 823 (2016) 70, doi: 10.3847/0004-637X/823/2/70.
[43] M.I. Mishchenko, L.D. Travis, D.W. Mackowski, T-matrix computations of light scattering by nonspherical particles: a review, J. Quant. Spectrosc. Radiat. Transf. 55 (1996) 535–575, doi: 10.1016/0022-4073(96)00002-7.
[44] P. Yang, K.N. Liou, Finite-difference time domain method for light scattering by small ice crystals in three-dimensional space, J. Opt. Soc. Am. A. 13 (1996) 2072, doi: 10.1364/JOSAA.13.002072.
[45] M. Fournier, P. Barritault, G. Jobert, A. Marchant, S. Boutami, J. Michelot, P. Lienhard, S. Nicoletti, L. Duraffourg, A miniaturized optical sensor for particulate matter detection, in: Y. Soskind, L.E. Busse (Eds.), Photonic Instrum. Eng. VII, SPIE, San Francisco, United States, 2020, p. 43, doi: 10.1117/12.2546128.
[46] S. Boutami, S. Nicoletti, Optical detector of particles, EP3574301 A1 2019-12-04 [EP3574301]-WO2018/138223 A1 2018-08-02 [WO2018138223]-FR3062209 A1 2018-07-27 [FR3062209]-KR10-2019-0112049A 2019-10-02 [KR20190112049], n.d. https://permalink.orbit.com/RenderStaticFirstPage?XPN=MV%252BDvbBf%252F0Euw56X k6cpNXfDUqlXTJ5uwQdFuycu4uk%3D%26n%3D1&id=0&base=.
[47] J. Michelot, P. Monsinjon, J. Caranana, A. Menard, M. Dubois, A. Lesire, C. Bouvier, S. Cohet, S. Caranhac, Creapyx: an Innovative Pixel Evaluation Platform, in: Toulouse, France, 2015. http://www.pyxalis.com/pyxalis-wp/wp-download/publications/2015_PYXALIS_CNES_CREAPYX.pdf.
[48] B. Dupont, J. Caranana, P.A. Pinoncely, J. Michelot, C. Bouvier, S. Cohet, P. Jourdain, P. Monsinjon, A dual-core highly programmable 120dB image sensor, Electron. Imaging. (2016) (2016) 1–3, doi: 10.2352/ISSN.2470-1173.2016.12.IMSE-261.
[49] E. Herth, M. Baranski, D. Berlharet, S. Edmond, D. Bouville, L.E. Calvet, C. Gorecki, Fast ultra-deep silicon cavities: toward isotropically etched spherical silicon molds using an ICP-DRIE, J. Vac. Sci. Technol. B. 37 (2019) 021206, doi: 10.1116/1.5081503.
[50] G. Jobert, M. Fournier, S. Boutami, C. Jamois, A. Lovera, D. Braga, C. Seassal, Y. Soskind, L.E. Busse, Millimeter-sized particle sensor using a wide field of view monolithic lens assembly for light scattering analysis in Fourier domain, Photonic Instrum. Eng. VII, SPIE, San Francisco, United States, 2020, p. 24, doi: 10.1117/12.2544185.
[51] G. Jobert, Optical particle detector, EP3598102 A1 2020-01-22 [EP3598102]-US20200033246 A1 2020-01-30 [US20200033246]-FR3083864 A1 2020-01-17 [FR3083864], n.d.https://permalink.orbit.com/RenderStaticFirstPage?XPN=o-Q9aRAtEpMKseLHW8WjXjnfDUqlXTJ5uwQdFuy-cu4uk%3D%26n%3D1&id=0&base=.
[52] P. Penttinen, K.L. Timonen, P. Tiittanen, A. Mirme, J. Ruuskanen, J. Pekkanen, Ultrafine particles in urban air and respiratory health among adult asthmatics, Eur. Respir. J. 17 (2001) 428–435, doi: 10.1183/09031936.01.17304280.
[53] J. Pribošek, G. Röhrer, Estimation of the particle sizing error due to particle position in an integrated PM2.5 optical particle counter, Proceedings 2 (2018) 850, doi: 10.3390/proceedings2130850.
[54] S.H. Jones, M.D. King, A.D. Ward, Determining the unique refractive index properties of solid polystyrene aerosol using broadband Mie scattering from optically trapped beads, Phys. Chem. Chem. Phys. 15 (2013) 20735, doi: 10.1039/c3cp53498g.
[55] A. Yevick, M. Hannel, D.G. Grier, Machine-learning approach to holographic particle characterization, Opt. Express. 22 (2014) 26884, doi: 10.1364/OE.22.026884.
[56] R.H. Zerull, R.H. Giese, K. Weiss, Scattering measurements of irregular particles Vs. MIE-theory, in: R.M.A. Azzam, D. Coffeen (Eds.), San Diego, 1977: pp. 191–199. 10.1117/12.955563.
[57] NASA GISS: Scattering – T-Matrix Codes, (n.d.). https://www.giss.nasa.gov/staff/mmishchenko/t_matrix.html(Accessed July 30, 2018).
[58] B. Mills, J. Grant-Jacob, S. Jain, Y. Xie, B. MacKay, M. McDonnell, M. Praeger, M. Loxham, D. Richardson, R. Eason, Particulate sensing using optical fibres and deep learning (Conference Presentation), in: K. Kitayama, B. Jalali (Eds.), AI Opt. Data Sci., SPIE, San Francisco, United States, 2020, p. 27, doi: 10.1117/12.2543951.
[59] P.B. Catrysse, X. Liu, A. El Gamal, QE reduction due to pixel vignetting in CMOS image sensors, Proc SPIE, 2000, pp. 420–430.

Gabriel Jobert received the Engineering degree and the MSc degree in Photonics & Microelectronics from Grenoble Institute of Technology and University Grenoble-Alpes, in 2017. He previously worked on 'in-vivo' laser-scanning imaging systems at the Interdisciplinary Laboratory of Physics (CNRS) and on optronic characterizations on cooled HdCdTe infrared image sensors at Sofradir (now Lynred). He is currently working at CEA-Leti and Institut des Nanotechnologies de Lyon (INL) as a PhD student where he develops miniature optical environmental sensors.

Pierre Barritault is an engineer in photonics at CEA-Leti. He graduated from the Institut d'Optique Graduate School (Paris Tech) in 1998. From 1999 to 2002, he prepared a thesis in a laboratory specialised in optical thin films coating (CEA Grenoble, France). This thesis, which was defended in October 2002, dealt with the theoretical and experimental study of the fluorescence of surface-bound molecules. For the past eight years, he has been working in the field of infrared gas sensors, on the design and development of NDIR gas sensors and also on the characterisation of QCL based gas sensors. For the past two years, he has developed and characterized a new type of Particulate Matter Sensors based on imaging of scattered light by a drilled imager.

Maryse Fournier received the Graduation degree from the Conservatoire National des Arts et Metiers, Grenoble, France, in 1993. She worked for 10 years at Sofradir (now Lynred) company where she was in charge of the flip-chip assembly of cooled infrared focal planes. In 2000, she joined CEA-Leti to develop processes and electro-optical characterizations of advanced infrared detectors. From 2010 to 2015, she has been working in the 200 mm CMOS foundry to develop Silicon Photonics devices for data and telecoms applications. She is currently a project coordinator and a process integration manager to develop sensors devices, as PM, chemical, bio-photonics, sensors for spectroscopic or life science applications.

Salim Boutami received his Engineering and PhD degrees in electrical engineering from the Ecole Centrale de Lyon, France, in 2004 and 2007 respectively. Since 2007, he has been a researcher at the Optronics Division of CEA-Leti, Grenoble, France, working on computational electromagnetism for photonics design. In 2017-2018, he was a visiting scholar in Professor Shanhui Fan's group at Stanford University. He has authored and co-authored about 40 articles in peer-reviewed journals, filed about 85 patents, and written one book. He was acknowledged in both 2016 and 2017 as 1st inventor of CEA, France.

Daphnée Jobert is graduating for the Signals and Image Processing, Communications and MultiMedia Engineering degree from Grenoble Institute of Technology, to be delivered by in 2020. She previously worked on image processing for a fine particle sensor based on the principle of lens-less optical scattering imaging at CEA-Leti. She is currently working at the University of Lausanne where she develops an automated debris size measurement, applied to UAV images in Alpine environment.

Adrien Marchant graduated from the University of Lille in 2014 with a Master degree specialized in lasers and spectroscopy applications. He previously worked as an R&D Engineer at Horiba Scientific for Coherent Raman imaging. In 2015, he developed automated optical instruments for multidrug-resistant bacteria diagnostic with Raman spectroscopy at Bioaster microbiology research institute. From 2015 to 2019, he performed MWIR and LWIR photonic components spectroscopic characterizations at CEA-Leti. In 2020, he joined Lynred where he works as Optical Validation Engineer for infrared focal plane arrays for aerospace applications.

Julien Michelot received his Ph.D. from Grenoble Institute of Technology in Micro and Nanoelectonics in 2012. During his Ph.D. thesis, he developed vertically pinned photodiode for in-depth charge storage in small pitch pixels for STMicroelectronics. In 2012, he joined Pyxalis, a CMOS image sensor design company where he is currently in charge of the development of innovative imaging solution for various application fields.

Paul Monsinjon received his Master of Engineering in Electrical and Electronic in 2010, from the Rennes National Institute of Technology and the Strathclyde University (Scotland, UK). Starting as a digital hardware designer, he joined the Characterization and Application few years later at Pyxalis, a CMOS image-sensor company. He still occupies this position and leads the characterization team from 2017.

Pierre Lienhard received his engineering graduation in 2013 and entered the CEA Grenoble as PhD student on the characterization and modelling of organic photodiodes ageing. After his defense in 2016, he shortly joined Lynred-former Sofradir company in the space division. He currently works at Pyxalis, a CMOS image sensor design company, since 2018 as part of the characterization team.

Sergio Nicoletti received the Ph.D. degree in 1996 working on HTc superconducting devices. From 1997 he was at CNR-IMM (Italy) working on Smart Sensors/Systems for air quality monitoring. In 2004, he took a visiting scientist position at HGST in San Jose, CA, USA, working on magnetic recording heads devices. In 2006, he joined CEA-LETI MINATEC to work on "Sensors and Optical Architectures for Chemical Detection" activity. Since then he has contributed to several proposals, now part of the projects portfolio of this activity. He owns more than 20 patents and more than 65 publications in peer-reviewed journals. He is now coordinating the H2020-MIRPHAB pilot line initiative.